Sequence of bifurcations of natural convection of air in a laterally heated cube with perfectly insulated horizontal and spanwise boundaries

Alexander Gelfgat [*]

School of Mechanical Engineering, Faculty of Engineering, Tel-Aviv University,
Ramat Aviv, Tel-Aviv 6997801, Israel

A sequence of three steady-oscillatory transitions of buoyancy convection of air in a laterally heated cube with perfectly thermally insulated horizontal and spanwise boundaries is studied. The problem is treated by Newton and Arnoldi methods based on Krylov subspace iteration. The finite volume grid is gradually refined from 100^3 to 256^3 finite volumes. It is shown that the primary instability is characterized by two competing eigenmodes, whose temporal development results in two different oscillatory states that differ by their symmetries. Bifurcations due to both modes are subcritical. These modes develop into different oscillatory and then chaotic flow states which, at larger Grashof number, stabilize and arrive to single stable steady flow. With further increase of the Grashof number, this flow loses its stability again. It is argued that, in all the three transitions, the instability onsets as well as reinstatement of stability take place owing to an interaction between a destabilizing centrifugal mechanism and stabilizing effect of thermal stratification.

I. INTRODUCTION

The primary goal of this paper is to examine a chain of three steady-oscillatory bifurcations that take place in a three-dimensional (3D) benchmark configuration of natural convection of air in a laterally heated cube with perfectly insulated horizontal and spanwise boundaries. The two-dimensional (2D) analog of this problem, i.e., convection in a square laterally heated cavity with perfectly thermally insulated (adiabatic) horizontal boundaries, is one of the earliest Computational Fluid Dynamics (CFD) benchmarks [1] proposed for validation of steady flow calculations. It was then extended for comparison of calculated critical parameters of the primary bifurcation corresponding to steady-oscillatory transition. The details and additional references can be found in Ref. [2]. Later, the 2D problem was extended to a 3D one in a cube, assuming the spanwise boundaries to also be perfectly thermally insulated. The results for 3D steady flows have been published and cross-verified [3–8], so that the 3D steady-flow benchmark is also well established. However, numerical investigation of the instabilities of 3D steady flows is significantly more challenging and has only been addressed by straightforward time integration of the 3D time-dependent governing equations [9–14].

Recently, a comprehensive linear stability analysis was applied to the primary steady-oscillatory transition of air convection in a laterally heated cube in two simpler configurations: for a cube with perfectly thermally conducting horizontal and spanwise boundaries [15], and with perfectly insulated horizontal and perfectly conducting spanwise boundaries [16]. The second case appeared to be noticeably more complicated because the critical Grashof number becomes almost two orders of magnitude larger, and the steady-oscillatory transition is preceded by a symmetry-breaking steady bifurcation. A replacement of the perfectly conducting spanwise boundaries by the perfectly

---

[*] gelfgat@tau.ac.il

insulated ones leads to a qualitatively different transition, which exhibits a sequence of bifurcations described below. This finding is in line with a recent computational and experimental study [17], where the authors concluded that the flow can be stabilized or destabilized by variation of the heat transfer conditions at the horizontal boundaries.

The time-dependent calculations in Ref. [14] showed that, with the increase of the Grashof number Gr, the steady flow becomes oscillatory unstable at $\text{Gr} > 4 \times 10^7$, then the stability reinstates at $\text{Gr} > 7 \times 10^7$, and the resulting steady flow becomes oscillatory unstable at $\text{Gr} > 2 \times 10^8$. Following a series of the above-cited previous studies, we consider the fixed value of the Prandtl number $\text{Pr} = 0.71$ characteristic for air. Flows with very large [18] and very small [19,20] Prandtl numbers were also considered for the current configuration; however, dependence of the transition on the Prandtl number is out of the scope of this paper.

In this paper, we examine the instabilities by applying a linear stability analysis, using the numerical approach and the visualization technique in Refs. [15,16]. For calculation of steady flows, we apply the Newton method, whose corrections are calculated by the biconjugate gradient stabilized [BiCGstab(2)] method combined with the generalized minimal residual (GMRES) method. Leading eigenvalues are computed by the Chebyshev preconditioned Arnoldi iteration [21]. The corresponding Krylov vectors, which are divergence free and satisfy all the boundary conditions, are computed by the SIMPLE-like technique proposed in Refs. [15,22].

Applying the linear stability analysis to the calculated 3D steady flows, we confirm three transitions predicted by the time-dependent computations [14]. We discuss which physical mechanisms destabilize the flow, then stabilize it, and then destabilize it again. Along with that, we confirm the existence of two different most unstable modes of the primary instability, as was predicted in Ref. [11]. We show that these modes differ by broken flow symmetries and become unstable at close Grashof numbers. Additional time-dependent calculations revealed that, beyond the stability limits, there exist two different oscillatory flow states which also differ by their symmetries. It was also shown that the steady-oscillatory transitions caused by either of the two modes are subcritical. With further increase of the Grashof number, these modes turn into chaotic regimes with different phase space attractors. Surprisingly, when the Grashof number is increased to $\sim 7 \times 10^7$, the two attractors collapse into the same stable focus, thus producing a single, stable, steady flow state. This flow state remains stable up to the Grashof number $\approx 2.9 \times 10^8$, after which the flow becomes oscillatory and then turbulent.

Analyzing the most unstable disturbances and steady flow patterns near the critical points, we argue that, in all three cases, the destabilization and stabilization result from an interaction of two main factors: the destabilizing centrifugal instability mechanism and stabilizing thermal stratification. The centrifugal instability sets in at the cube corners where the flow direction turns from horizontal to vertical, and vice versa, like what is observed in the 3D lid driven cavity flow (see Ref. [22] and references therein). This mechanism can be enhanced by reverse circulations that appear near the top and bottom borders and increase the curvature of streamlines of the main convective circulation. On the other hand, strong convective mixing tends to make the isotherms far from the vertical isothermal boundaries almost horizontal, so that colder and heavier fluid is located below warmer and lighter fluid. This results in a stable stratification which tends to suppress all possible instabilities.

II. FORMULATION OF THE PROBLEM

As in our previous studies [14–16], we consider the natural convection of a Boussinesq fluid in a cubic cavity with the side length H, whose opposite sidewalls are maintained at constant but different temperatures T_{hot} and T_{cold}. The horizontal and spanwise boundaries are perfectly thermally insulated, as is defined for the AA–AA case in Ref. [14]. To render equations dimensionless, we choose H, H^2/ν, ν/H, and $\rho \nu^2/H^2$ as scales of the length, time t, the velocity $\boldsymbol{v} = (u, v, w)$, and the pressure p, respectively, where ν is the fluid kinematic viscosity and ρ is the density. The temperature is rescaled to a dimensionless function by $T \rightarrow (T - T_{\text{cold}})/(T_{\text{hot}} - T_{\text{cold}})$. Additionally,

the dimensionless time, velocity, and pressure are scaled, respectively, by $\mathrm{Gr}^{-1/2}$, $\mathrm{Gr}^{1/2}$, and Gr, where $\mathrm{Gr} = g\beta(T_{\mathrm{hot}} - T_{\mathrm{cold}})H^3/\nu^2$ is the Grashof number, g is the acceleration due to gravity, and β is the thermal expansion coefficient. The resulting system of energy, momentum, and continuity equations is defined in a cube $0 \leqslant x, y, z \leqslant 1$ as

$$\frac{\partial T}{\partial t} + (\boldsymbol{v} \cdot \nabla)T = \frac{1}{\mathrm{PrGr}^{1/2}}\Delta T, \tag{1}$$

$$\frac{\partial \boldsymbol{v}}{\partial t} + (\boldsymbol{v} \cdot \nabla)\boldsymbol{v} = -\nabla p + \frac{1}{\mathrm{Gr}^{1/2}}\Delta \boldsymbol{v} + T\boldsymbol{e}_z, \tag{2}$$

$$\nabla \cdot \boldsymbol{v} = 0, \tag{3}$$

where $\mathrm{Pr} = \nu/\alpha$ is the Prandtl number, and α is the thermal diffusivity. All the boundaries are assumed to be no-slip. Two vertical boundaries at $x = 0, 1$ are kept isothermal, so that

$$T(x = 0, y, z) = 1, \quad T(x = 1, y, z) = 0. \tag{4}$$

The absence of the heat flux at the horizontal and spanwise boundaries yields

$$\left(\frac{\partial T}{\partial y}\right)_{y=0} = \left(\frac{\partial T}{\partial y}\right)_{y=1} = 0, \tag{5}$$

$$\left(\frac{\partial T}{\partial z}\right)_{z=0} = \left(\frac{\partial T}{\partial z}\right)_{z=1} = 0. \tag{6}$$

For discussion purposes, the areas adjacent to the cube edges (0,y,0), (0,y,1), (1,y,0), and (1,y,1) are called below the lower left, upper left, lower right, and upper right corners, respectively.

The problem is additionally characterized by three symmetries [11]: (i) reflection symmetry with respect to the midplane $y = 0.5$, $\{u, v, w, \theta\}(x, y, z) = \{u, -v, w, \theta\}(x, 1 - y, z)$, (ii) 2D rotational symmetry with respect to rotation through $180°$ around the line $x = z = 0.5$, $\{u, v, w, \theta\}(x, y, z) = -\{u, -v, w, \theta\}(1 - x, y, 1 - z)$, and (iii) 3D centrosymmetry $\{u, v, w, \theta\}(x, y, z) = -\{u, v, w, \theta\}(1 - x, 1 - y, 1 - z)$, where $\theta = T - (1 - x)$. Obviously, these symmetries characterize steady-state flows at relatively small subcritical Grashof numbers. They can be broken by instability, so that supercritical oscillatory flows can maintain only one type of symmetry or be fully nonsymmetric. Following Ref. [16], to examine whether the steady-state solution is symmetric, we use the temperature field and define

$$R_{\mathrm{ref}} = \max|\theta(x, y, z) - \theta(x, 1 - y, z)|, \tag{7}$$

$$R_{\mathrm{2D}} = \max|\theta(x, y, z) + \theta(1 - x, y, 1 - z)|, \tag{8}$$

$$R_{\mathrm{3D}} = \max|\theta(x, y, z) + \theta(1 - x, 1 - y, 1 - z)| \tag{9}$$

as measures of the reflection, 2D rotational, and 3D centrosymmetries, respectively. For the symmetric numerical solutions, these values are of the order of 10^{-9}. Deviation of any of these expressions from numerical zero indicates symmetry breaking.

III. NUMERICAL AND VISUALIZATION TECHNIQUES

The numerical approach is the same as in Refs. [14–16], where the reader is referred for the details. Here, we only mention that this approach allows for calculation of divergence-free Krylov vectors satisfying all the boundary conditions, which in its turn allows for a direct calculation of the leading eigenvalue [21], without applying the Arnoldi method in shift-and-inverse mode like in Ref. [23].

As mentioned in Ref. [16], convergence of the critical parameters for a similar 2D case of convection in a laterally heated square cavity with insulated horizontal boundaries was established in Ref. [23], the convergence and comparison with independent results for 3D steady states were
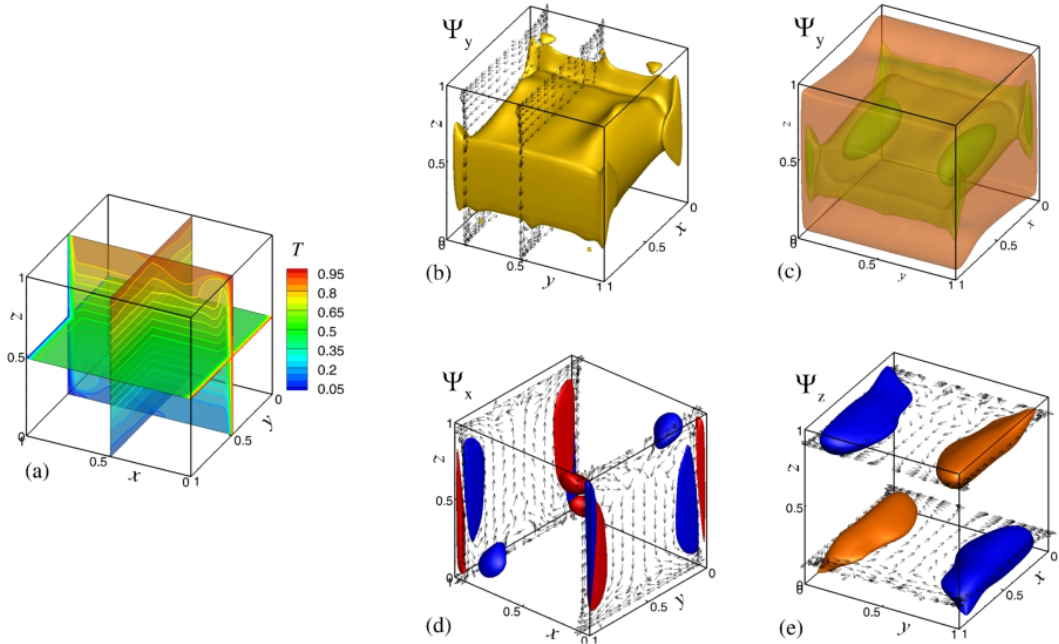
FIG. 1. (a) Visualization of a subcritical steady three-dimensional (3D) flow at $Pr = 0.71$, $Gr = 4.4 \times 10^7$ by isotherms and (b)–(e) divergence-free projections of the velocity field on the coordinate planes. The projected velocity fields are depicted by vectors. Isosurfaces of the velocity potentials, to which the projected velocities fields are tangent, are shown by colors. The minimal and maximal values of the potentials are ± 0.00205, $(-0.00982, 0.000226)$, and ± 0.00339 for Ψ_x, Ψ_y, and Ψ_z, respectively. The isosurfaces are plotted for the levels (b) -0.004 and (c) -0.0025, -0.0065, and -0.009 for Ψ_y; (d) ± 0.0008 for Ψ_x; and (e) ± 0.0012 for Ψ_z.

reported in Ref. [8], and the convergence of slightly supercritical oscillatory states was studied in Ref. [14].

3D velocity fields are visualized by the method proposed in Refs. [24,25] and applied to similar problems in Refs. [15,16], where all the definitions and computational details are discussed. Here, to clarify the plots below, we only mention that 3D flow is visualized by projecting the velocity field on three sets of coordinate planes (x,y), (y,z), and (x,z), demanding that the projections are divergence free. Each of the three divergence-free projections has only two nonzero components along the coordinates of the projection plane, which allows one to define a stream function for each of them. As a result, the 3D velocity field is visualized as isosurfaces of the three scalar functions Ψ_x, Ψ_y, and Ψ_z, which are nonzero components of the vector potentials of the above projections. The visualization of a divergence-free 3D velocity field consists of three independent frames depicting the vector potentials and the velocity projections. The whole visualization approach can be considered an extension of a 2D stream function to three directions, in which the velocity projection vectors are tangent to the isosurfaces of the corresponding vector potential.

Before discussing the 3D flow patterns, we recall that, in a laterally heated 3D cavity, the flow is always three-dimensional [2,19,26]. It is characterized by a strong convective circulation in the planes located between the isothermal boundaries and a noticeably weaker motion in the two other sets of vertical and horizontal planes. The weaker motion in the spanwise direction is driven by the pressure drop between the vertical center plane and the spanwise boundaries. At the center plane, the velocities are expected to be maximal, vanishing toward the spanwise boundaries due to the no-slip boundary conditions. Consequently, the pressure grows from the center to the spanwise boundaries, which results in the flow from the center toward these boundaries.
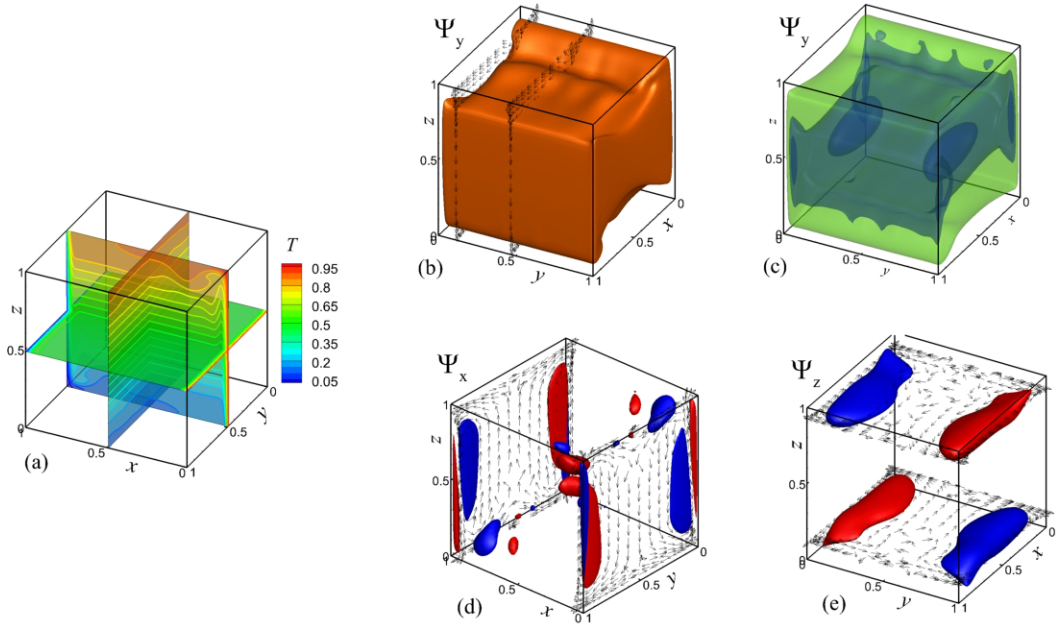
FIG. 2. (a) Visualization of a subcritical steady three-dimensional (3D) flow at Pr = 0.71, Gr = 7.2×10^7 by isotherms and (b)–(e) divergence-free projections of the velocity field on the coordinate planes. The projected velocity fields are depicted by vectors. Isosurfaces of the velocity potentials, to which the projected velocities fields are tangent, are shown by colors. The minimal and maximal values of the potentials are ± 0.00200, $(-0.00878, 0.000226)$, and ± 0.00308 for Ψ_x, Ψ_y, and Ψ_z, respectively. The isosurfaces are plotted for the levels (b) -0.0004 and (c) -0.0025, -0.0065, and -0.008 for Ψ_y; (d) ± 0.0008 for Ψ_x; and (e) ± 0.0012 for Ψ_z.

Figures 1–3 illustrate the above visualization approach for steady flows at three values of the Grashof number Gr = 4.4×10^7 (Fig. 1), Gr = 7.2×10^7 (Fig. 2), and Gr = 2.9×10^8 (Fig. 3), which are close to the critical values of the three transitions discussed below. In all the three cases, the steady flows preserve all three symmetries. Like what was discussed in Refs. [14,15], the main convective circulation is created by motion in the (x, z) planes and is represented by the vector potential Ψ_y: the hot air ascends and the cold air descends along its isosurfaces. Frames (c) in Figs. 1–3 show that, at large Grashof numbers, the central part of the main circulation splits into two [Figs. 1(c) and 2(c)] and then into three [Fig. 3(c)] separate circulations. Motion in the (y, z) planes is represented by the isosurfaces of the potential Ψ_x, which show that this motion takes place mainly in the boundary layers adjacent to the isothermal boundaries $x = 0$ and 1. Similarly, the motion in the (x, y) planes is visualized by the isosurfaces of the potential Ψ_z. This motion is located mainly near the horizontal boundaries, showing existence of a boundary layer there also. Arrow plots in Figs. 1–3 are tangential to the isosurfaces and illustrate the direction of the divergence-free velocity projections.

It should be noted additionally that, unlike the AA–CC case [14,16] of perfectly conducting spanwise boundaries, the temperature isosurface pattern does not exhibit any boundary layers or other steep dependencies near the perfectly insulated spanwise boundaries. Thus, in the central plane $x = 0.5$, the isotherms are almost horizontal and exhibit a visible waviness only near the horizontal boundaries. We also observe that the intensive convective motion brings the cold liquid below and the warm liquid above, so that the isotherms shown in Figs. 1(a)–3(a) exhibit a clear stable stratification, which is expected to affect the flow stability.
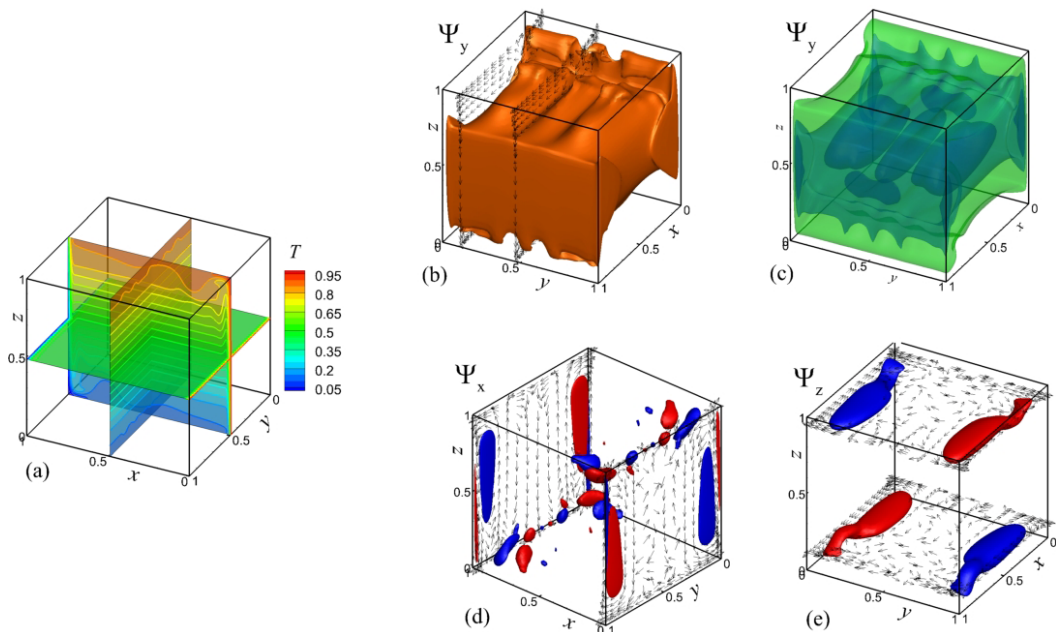
FIG. 3. (a) Visualization of a subcritical steady three-dimensional (3D) flow at $Pr = 0.71$, $Gr = 2.9 \times 10^8$ by isotherms and (b)–(e) divergence-free projections of the velocity field on the coordinate planes. The projected velocity fields are depicted by vectors. Isosurfaces of the velocity potentials, to which the projected velocities fields are tangent, are shown by colors. The minimal and maximal values of the potentials are ± 0.00174, $(-0.00642, 0.000838)$, and ± 0.00247 for Ψ_x, Ψ_y, and Ψ_z, respectively. The isosurfaces are plotted for the levels (b) -0.004 and (c) -0.0025, -0.0045, and -0.0055 for Ψ_y; (d) ± 0.0009 for Ψ_x; and (e) ± 0.0012 for Ψ_z.

IV. RESULTS

A. Critical Grashof numbers and oscillation frequencies

Convergence of the critical Grashof numbers and critical frequencies was studied on gradually refined grids varied from 100^3 to 256^3 finite volumes. The grids were stretched near the borders as in Refs. [14–16]. The critical values corresponding to the three consequent bifurcations exhibited a linear dependence on the squared average size grid, like what is illustrated in fig. 4 in Ref. [15]. This allowed us to perform the Richardson extrapolation [27] and to find zero grid size limits of the critical Grashof numbers and critical frequencies. All the results are listed in Table I.

The primary bifurcation takes place at $Gr_{cr} \approx 4.50 \times 10^7$. The corresponding most unstable perturbation exhibits broken reflection symmetry and 3D centrosymmetry but preserves the 2D rotational symmetry. Along with this most unstable perturbation mode, we observed another mode which becomes unstable at $Gr \approx 4.52 \times 10^7$. It preserves 3D centrosymmetry and breaks the two other symmetries. The retaining of the 3D centrosymmetry with the two other symmetries broken was already observed and discussed in Refs. [14,16]. The critical Grashof numbers of these two modes are so close that, to arrive at a correct critical value, it was necessary to observe four leading eigenvalues. These two modes were observed before in Ref. [11], but other studies [9,10,12–14] reported only one of them.

The computed critical parameters are compared with previously published results in Table I. Parameters of the second and third bifurcations can be compared only with the results of Ref. [14]. Considering difficulties in estimating of the critical Grashof number from results of a time-dependent calculation, the comparison is quite good. The present critical Grashof numbers

TABLE I. Present linear stability results compared with the previous ones obtained by the time-dependent calculations.

Reference	Method	$\text{Gr}_\text{cr} \times 10^{-7}$	f_cr
	First bifurcation		
Janssen and Henkes (1995) [9]	120^3 finite volume grid	3.5–5.6	0.01
Labrosse *et al.* (1997) [10]	61^3 collocation points	4.79	0.00488
De Gassowski *et al.* (2006) [11]	80^3 collocation points	4.46	0.00502
		4.52	0.00919
Soucasse *et al.* (2014) [13]	80^3 collocation points	4.4–4.9	0.0067
Gelfgat (2017) [14]	256^3 finite volume grid	4.58	0.0107
This paper	256^3 finite volume grid, linear stability analysis	4.504	0.00504
		4.517	0.00791
	Second bifurcation		
Gelfgat (2017) [14]	256^3 finite volume grid	7.2	0
This paper	256^3 finite volume grid, linear stability analysis	7.095	0
	Third bifurcation		
Gelfgat (2017) [14]	256^3 finite volume grid	28.0	0.525
This paper	256^3 finite volume grid, linear stability analysis	29.59	0.531

corresponding to the two modes of the primary bifurcation coincide within the second decimal place with the independent calculations [11], while only the first decimal place is the same for other results. The scatter is noticeably larger in the reported oscillation frequencies. The discrepancy between the present results and those of time-dependent computations in Ref. [11] can possibly be explained by change of the oscillations period in slightly supercritical flows. The oscillation frequencies reported in other studies cited in Table I can result either from interaction of the two unstable modes or from the subcriticality of the primary bifurcation, discussed below. Note that the dimensionless frequency ≈ 0.01, reported in three studies [9,11,14], can be interpreted as one resulting in finite amplitude oscillations of the second primary mode, whose critical frequency obtained here is ≈ 0.008.

B. Primary steady-oscillatory transition

1. Perturbations of temperature: Comparison with 2D case and fully nonlinear time-dependent computations

As mentioned above, the primary steady-oscillatory transition takes place at $\text{Gr}_\text{cr} \approx 4.5 \times 10^7$ owing to a 2D rotational symmetry-preserving perturbation, which breaks two other symmetries. This is accompanied by another 2D rotational symmetry and reflection symmetry-breaking eigenmode which becomes unstable at $\text{Gr} \approx 4.52 \times 10^7$ and bifurcates from the same single steady-state branch. Starting from a quite small supercriticality, e.g., $\text{Gr} = 4.55 \times 10^7$, there exist two competing eigenmodes, so that one can expect to observe interaction of the two modes as well as two distinct oscillatory states developing independently owing to either of the modes.

Before addressing the slightly supercritical flow states, we compare the 3D instability of the considered flow with its 2D counterpart (see, e.g., Ref. [23]), with the distribution of oscillation amplitude in a fully developed slightly supercritical 3D oscillatory state in the cube [14], and with the amplitude reported for 3D instability of the 2D flow with the spatially periodic spanwise boundary conditions [28]. Figures 4(a)–4(d) show perturbations of the temperature of both modes as
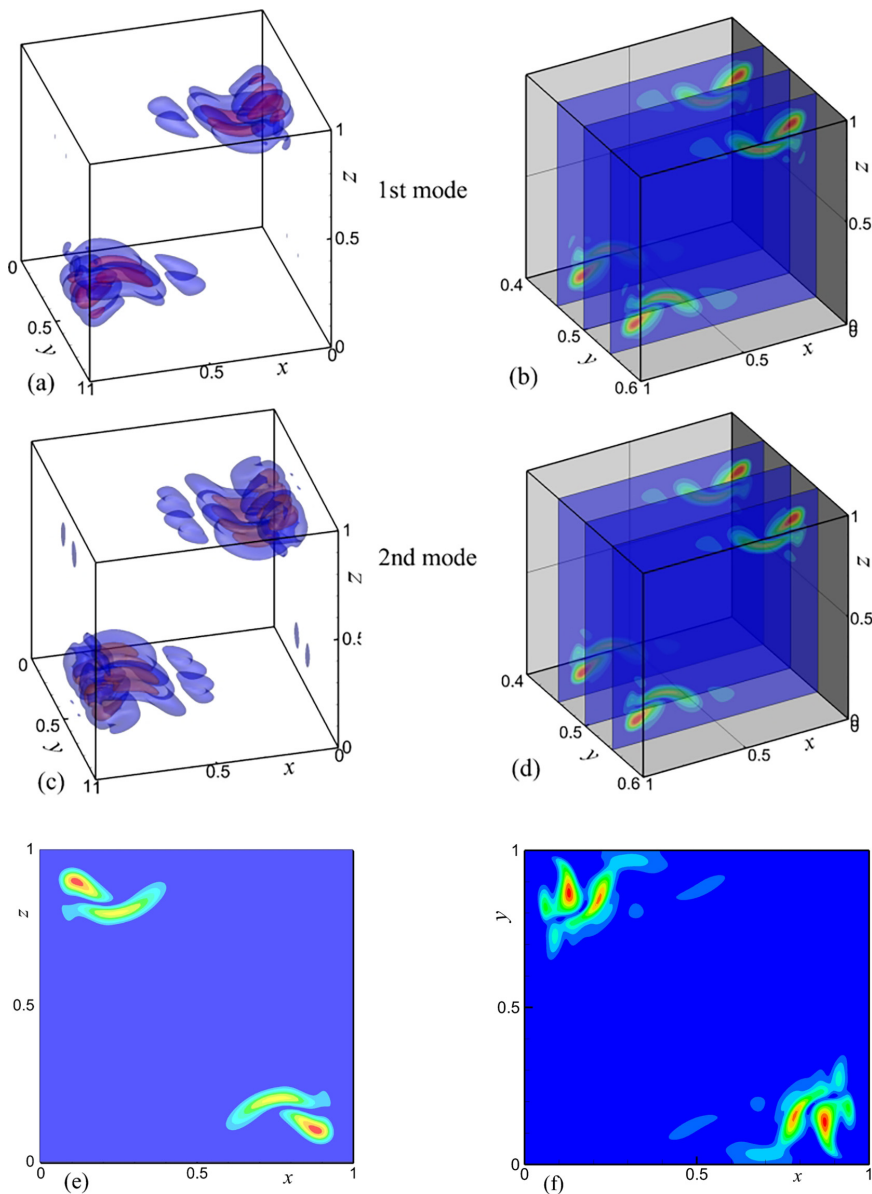
FIG. 4. Amplitude of two modes of the temperature perturbation of the primary bifurcation. (a) and (c) Isosurfaces. (b) and (d) Amplitude of the temperature perturbation in several $y = $ const. planes of (a) and (c). The isosurfaces in (a) and (c) are plotted for the levels of 10% and 40% of the maximal amplitude, which are 0.00585 and 0.00474 for the first and second modes, respectively. (e) Amplitude of the slightly supercritical oscillatory two-dimensional (2D) flow. (f) Amplitude of the most unstable mode of the temperature perturbation in the 2D AA case, $Gr_{cr}^{(2D)} = 2.42 \times 10^8$. (b), (d), (e), and (f) show 10 equally distanced levels.

isosurfaces [frames 4(a) and 4(c)] and isolines in the central plane $y = 0.5$ and two neighbor planes $y = 0.45$ and 0.55 [frames 4(b) and 4(d)]. For comparison purposes, we also show amplitudes of the oscillatory 2D flow [Fig. 4(e)] and the most unstable 2D disturbance [Fig. 4(f)]. The 3D patterns should be compared with those plotted in fig. 12 in Ref. [14]. We observe that the amplitudes of

the perturbations and the oscillations in all the 2D and 3D cases are located in the same corners $x = z = 0$ and $x = z = 1$ and exhibit quite similar patterns. At the same time, one can observe different structures shape in the 2D and 3D disturbances. Moreover, in the case of similar 2D and 3D instability mechanisms, the similarity is expected to be observed in the center plane $y = 0.5$, like in Ref. [15]. In the present case, the temperature disturbance is zero at the center plane [Fig. 4(b) and 4(c)] and attains the maximal values in the nearby planes. Comparing also isosurfaces of the amplitudes of both modes with the oscillation amplitude of the supercritical oscillatory state (fig. 12a in Ref. [14]), we observe similarity. The difference in the patterns can be attributed to the changes due to nonlinear development of the oscillatory flow. For example, appearance of noticeable oscillations in the two opposite corners $x = 0$, $z = 1$ and $x = 1$, $z = 0$ can trigger a strong nonlinear effect. The similarity is seen better in the cross-sectional planes (cf. Figs. 4(b) and 4(d) with fig. 12c in Ref. [14]). There is also certain similarity between the discussed amplitudes of perturbations and oscillatory flows with the Proper Orthogonal Decomposition (POD) empirical eigenfunctions reported in fig. 3 in Ref. [29].

An additional comparison can be made with the results of 3D instability onset in a 3D cavity with the periodic spanwise boundary conditions and the 2D base flow [28]. The 3D instability reported in Ref. [28] is found to occur via a steady bifurcation with the spanwise wave number 19.2, which corresponds to the spanwise width ratio 0.327. Apparently, the bifurcation type and the spanwise extent do not correspond to the present findings. At the same time, the pattern of the temperature disturbance amplitude (fig. 1 in Ref. [28]) is like the one plotted in Fig. 4. The similarity is revealed not only in the isolines shape but also in the fact that, in both cases, the perturbation vanishes in the central plane, which corresponds to the reflection symmetry breaking observed in both cases.

2. Two most unstable perturbation modes

For a better comparison of the two modes and an illustration of their symmetry properties, their real and imaginary parts are plotted in Fig. 5. We observe that, within a phase shift, the two modes exhibit similar patterns that consist of two or four pairs of minima and maxima located in the corners $x = z = 0$ and $x = z = 1$. It is clearly seen that the first mode preserves the 2D centrosymmetry, while it breaks the 3D centrosymmetry. Contrarily, the second mode preserves the 3D centrosymmetry and breaks the 2D rotational symmetry. Both modes are antisymmetric with respect to the center plane $y = 0.5$, meaning that both break the reflection symmetry. The time evolution of the two disturbances over the oscillation period is visualized in Animations 1 and 2 in the Supplemental Material [30]. Note also that the real and imaginary parts of the first mode [Figs. 5(a) and 5(b)] are well compared with those of the dominant dynamic mode decomposition mode reported in fig. 4 in Ref. [13].

Both most unstable modes have the largest amplitudes of the three velocity components in the lower left and upper right corners $x = z = 0$ and $x = z = 1$, where the temperature perturbation amplitude is also the largest (Fig. 5). Like the temperature disturbances, the oscillations of the velocity perturbation in time are located near these corners and do not penetrate further in the bulk of the flow (see Animations 1 and 2 in the Supplemental Material [30]). Since all the perturbations of both modes are located close to the isothermal boundaries $x = 0$ and 1, the corresponding boundary layers can play an important role in the onset of observed instabilities. A closer look at the steady flow patterns reveals that, indeed, there are extremely thin boundary layers of the vertical velocity and the temperature. The corresponding profiles in the spanwise midplane $y = 0.5$ are shown in Fig. 6. We observe the steepest change of the vertical velocity near the horizontal midplane $z = 0.5$ [Figs. 6(a) and 6(b)], while the steepest change of the temperature takes place near the isothermal boundaries [pink and green lines in Fig. 6(c)].

The observed boundary layers resemble the problem of natural convection in the boundary layer adjacent to a vertical heated plate [31]. Stability of this flow was examined in several studies [32,33], where only 2D perturbations were considered. This can be justified by the Squire transformation, which is applicable to parallel natural convection flows. In the present case, we observe the most
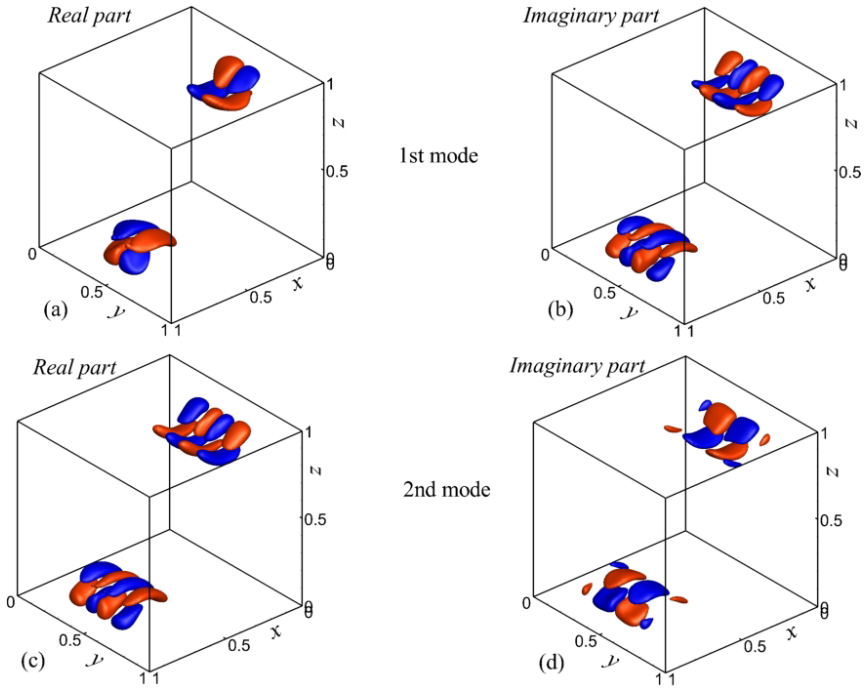
FIG. 5. Real and imaginary parts of two modes of temperature perturbation of the primary bifurcation. The isosurfaces are plotted for the levels ±0.001, while maximal amplitude values are 0.00585 and 0.00474 for the first and second modes, respectively. See Animations 1 and 2 in the Supplemental Material [30].
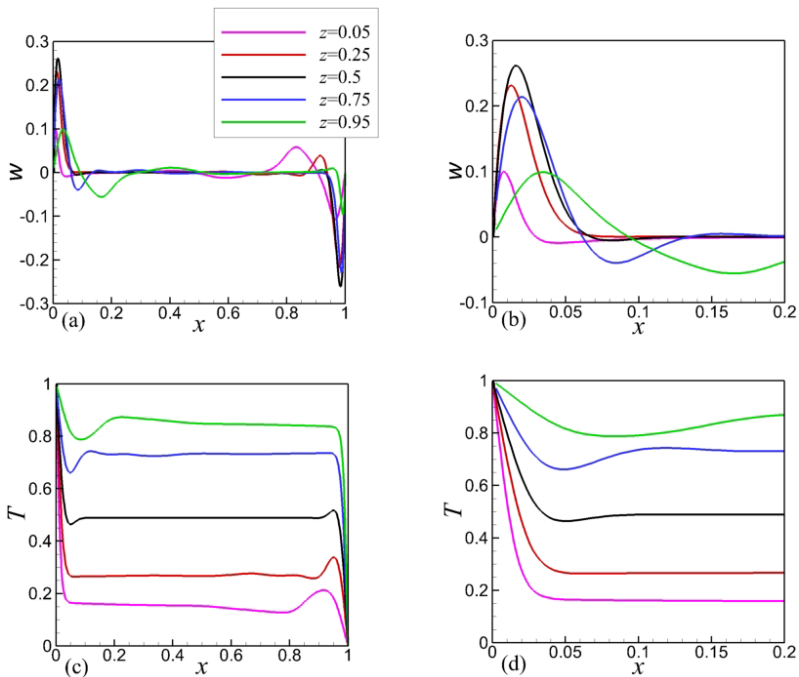

FIG. 6. Profiles of the vertical velocity and the temperature in the spanwise midplane $y = 0.5$. In (b) and (d), the profiles in the interval $0 \leqslant x \leqslant 0.2$ are zoomed. Gr $= 4.4 \times 10^7$.
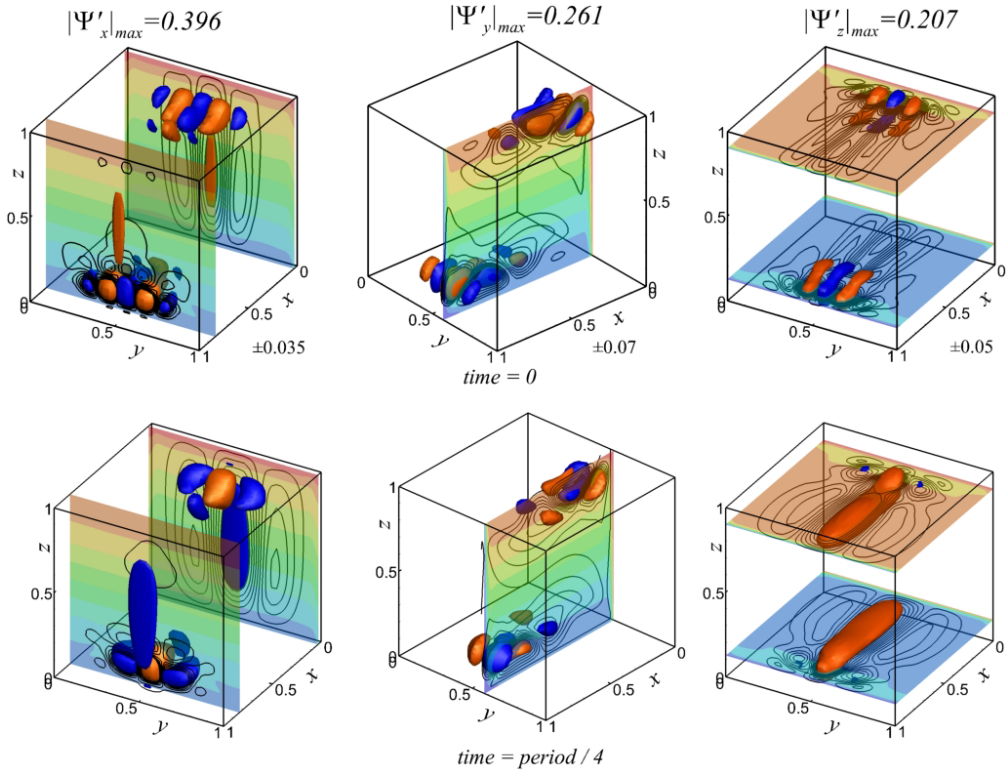
FIG. 7. Snapshots of the velocity potentials of the first most unstable perturbation. The minimal and maximal values and the plotted levels are shown in the upper frames. The snapshots at the $\frac{1}{2}$ and $\frac{3}{4}$ of the period can be obtained by reversing the colors. The color maps show the temperature field in the characteristic cross-sections. $Gr = 4.5 \times 10^7$. See Animation 3 in the Supplemental Material [30] for evolution of the perturbation potentials over the period.

unstable 3D disturbances (Fig. 5), which makes the above results inapplicable for explanation of the observed instability. It is still possible that, at large Grashof numbers, the most unstable perturbation of the parallel boundary layer flow will become 3D, like what was observed for nonisothermal mixing layer flows at large Richardson numbers in Refs. [34,35]. However, even in this case, one would expect disturbances distributed along the vertical boundaries and not just localized in the corners.

An additional understanding of the mechanism that triggers the instability can be gained from the snapshots of the vector potentials showing the divergence-free projections of the velocity disturbance on the coordinate planes. These are also shown for the first and second modes in Figs. 7 and 8, respectively. The snapshots are plotted for the beginning and for a quarter of an oscillation period. The corresponding patterns for half and three quarters of the period can be obtained by reversing the colors. The corresponding Animations 3 and 4 in the Supplemental Material [30] show 40 snapshots over an oscillation period. The projected motions are also depicted by their streamlines. The direction of motion on the streamlines changes to the opposite during the oscillation period.

The perturbation patterns shown in Figs. 5, 7, and 8 allow us to speculate about the physics of the two self-sustained oscillatory processes. First, we argue that, owing to the base flow symmetries, the flow areas adjacent to the corners $x = z = 0$ and $x = z = 1$ are equivalent with respect to the flow stability properties there. Therefore, the instability develops in both corners simultaneously, as is seen from the most unstable perturbation patterns (Fig. 5). Second, we observe (see, e.g., Fig. 5) that
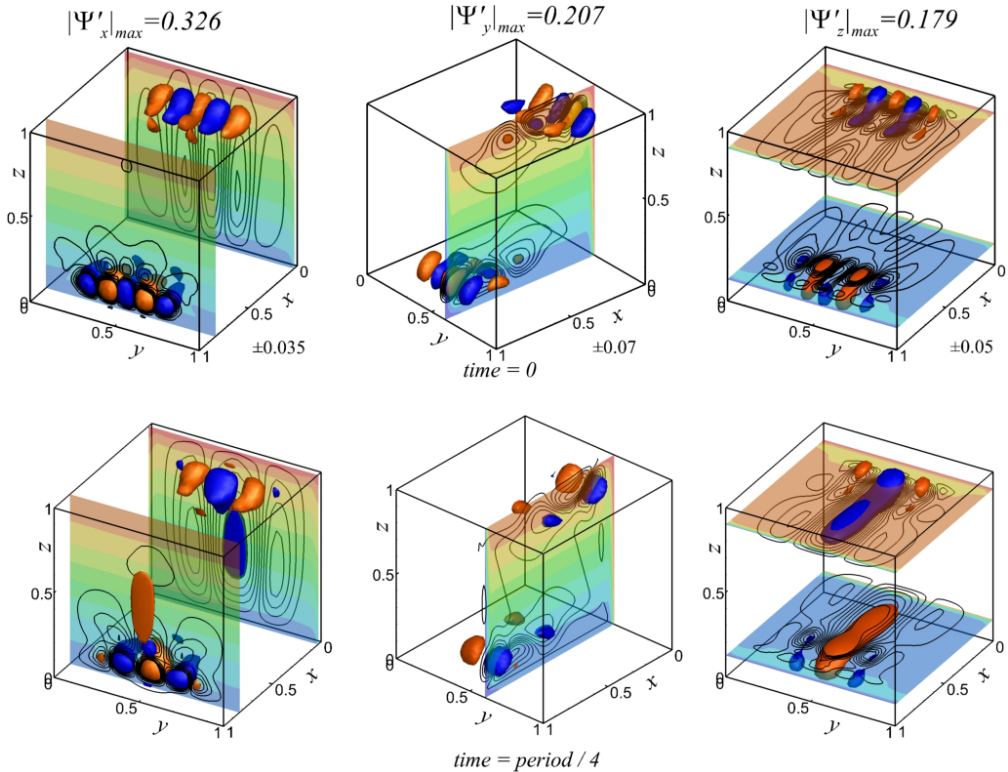
FIG. 8. Snapshots of the velocity potentials of the second most unstable perturbation. The minimal and maximal values and the plotted levels are shown in the upper frames. The snapshots at the $\frac{1}{2}$ and $\frac{3}{4}$ of the period can be obtained by reversing the colors. The color maps show the temperature field in the characteristic cross-sections. Gr $= 4.5 \times 10^7$. See Animation 4 in the Supplemental Material [30] for evolution of the perturbation potentials over the period.

both perturbations modes are antisymmetric with respect to the midplane $y = 0.5$, meaning that the reflection symmetry will always be broken by the instability. Third, the temperature disturbances shown in Fig. 5 can appear in phase with respect to the 2D rotation $(x, y, z) \rightarrow (1 - x, y, 1 - z)$, like mode 1, or in counterphase, like mode 2. In the latter case, the antisymmetry with respect to reflection and the 2D rotation leads to the symmetry with respect to the 3D rotation $(x, y, z) \rightarrow (1 - x, 1 - y, 1 - z)$. Note that the definition of the symmetries in Sec. II assumes a change of the sign of $\theta = T - (1 - x)$ under either of the rotations. Therefore, mode 1 breaks the 2D rotational symmetry, while mode 2 breaks the 3D centrosymmetry.

Seeking an explanation of this instability, we notice the complicated structure of similar flows in 2D cavities where, at large Grashof numbers, reverse circulations appear at the horizontal boundaries near the corners (see, e.g., fig. 2e in Ref. [36]). In the regions of these reverse circulations, several changes of sign of the vertical velocity along the x axis are observed. We also see these changes in the vertical velocity profiles of the present 3D solution (Fig. 6). The reverse circulations are difficult to recognize in the 3D velocity field; however, they can be revealed in the midplane streamlines plotted together with the absolute value of vector potential Ψ_y in Fig. 9 for the first mode in the cross-section $y = 0.5$. A similar plot can be drawn for the second mode. These reverse vortices increase the curvature of streamlines of the main circulation. As a result, the corner flow can become centrifugally unstable. This assumption is elaborated below. All the amplitudes of the absolute values (amplitudes) of vector potential of the most unstable velocity disturbance (Fig. 9)
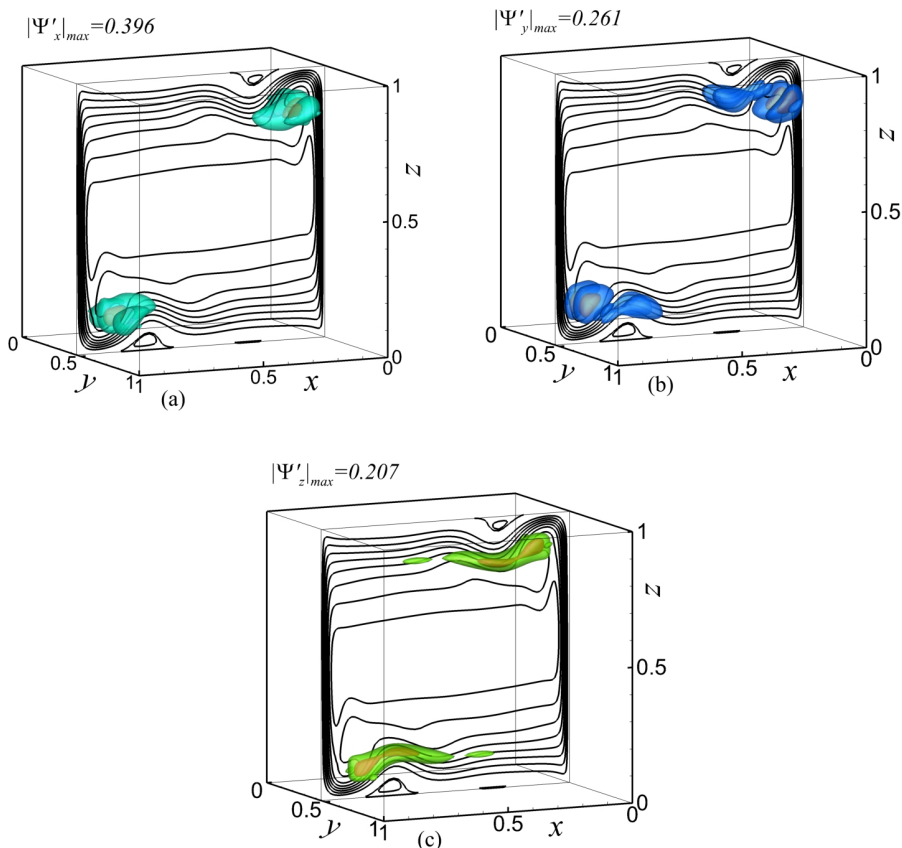
FIG. 9. Absolute values (amplitudes) of the velocity potentials of the first most unstable perturbation of the primary bifurcation (isosurfaces) and isolines of the base flow velocity potential Ψ_y plotted in the center plane $y = 0.5$ at $\mathrm{Gr_{cr}} \approx 4.5 \times 10^7$. Maximal levels of the amplitudes are shown in the graph. The isosurfaces are plotted for the levels (a) 0.028 and 0.1, (b) 0.012 and 0.2, and (c) 0.1 and 0.17.

are of comparable magnitude and are located in the areas of reverse circulations, which supports the assumption of centrifugal instability.

As mentioned above, appearance of the reverse circulations increases the isolines curvature in the corner regions, so that centrifugal instability mechanisms can be triggered there. To examine this possibility, we calculated the Rayleigh and Bayly criteria [37,38], as in Ref. [22]. Figure 10 shows the Rayleigh criterion, defined as $\eta = -\partial |\mathbf{r} \times \mathbf{v}|^2 / \partial r$, where the radius $\mathbf{r}$ is taken as the distance and direction from the center of main convective circulation. The latter is assumed to coincide with the maximum of the potential Ψ_y in the center plane $y = 0.5$ [22]. An inviscid instability is expected when η changes its sign from positive to negative, which clearly takes place, Fig. 10, in the corner areas we wish to examine.

The Bayly criterion R is calculated as in Refs. [22,39] using the equation:

$$R = \frac{|\mathbf{u}_{2D}|^3 \zeta}{(\nabla \Psi_y) \cdot [(\mathbf{u}_{2D} \cdot \nabla)\mathbf{u}_{2D}]}, \quad \text{where } \mathbf{u}_{2D} = \mathrm{rot}\Psi_y, \text{ and } \zeta = (\mathrm{rot}\mathbf{u}_{2D})_y. \tag{10}$$

The inviscid centrifugal instability is expected if R is negative somewhere in the flow. The pattern of the Bayly criterion R is like that of the Rayleigh criterion (Fig. 10) and is not shown. Its negative values appear in the corners where we observe the largest values of disturbances. Thus, both criteria
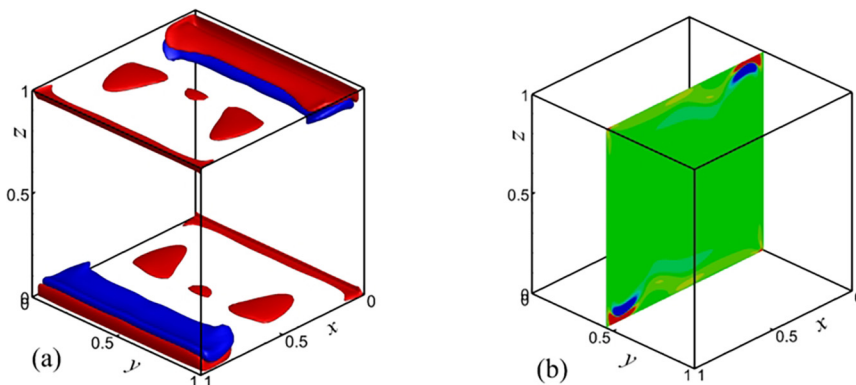
FIG. 10. Isolines of Rayleigh criterion calculated for the base flow at $Gr_{cr} \approx 4.5 \times 10^7$. The level values in (a) are ± 0.005. Positive and negative values are shown by the red and blue color, respectively.

indicate the possibility of the centrifugal instability; however, related to inviscid flows only, they do not prove it.

To argue additionally in favor of a possible centrifugal mechanism involved in the onset of the observed instability, we compute and plot divergence-free projections of the velocity field on the planes parallel and orthogonal to the diagonal plane connecting the lower left and upper right corners, as in Ref. [22] for the lid driven cavity flow. The new coordinate planes are defined by the coordinate rotation:

$$x' = \frac{x+z}{2}, \quad z' = \frac{x-z}{2}. \tag{11}$$

The results for both most unstable modes are shown in Fig. 11. The argument here is that the centrifugal instability results in the vortices rotating in the planes orthogonal to the initial plane of rotation like, e.g., in the Taylor-Couette flow. In Fig. 11, we observe such vortical structures rotating in the diagonal plane, while the initial rotating motion in the corners takes place in the planes $y = \mathrm{const}$.

Based on the above observations, we explain the onset of oscillatory instability and the resulting self-sustained oscillatory process as follows. The instability is triggered by the centrifugal mechanism in the corners $x = z = 0$ and $x = z = 1$. As discussed below, the instability in the opposite corners can develop in phase or in counterphase, giving rise to the two most unstable modes having close critical Grashof numbers. The centrifugally induced vortices (Fig. 11) transport colder and warmer fluid in warmer and colder locations, respectively, thus creating the localized temperature perturbations, as is observed in Fig. 5. Note that strong convective mixing by the base flow creates stable stratification in most of the bulk of the flow (Fig. 2), except the isothermal vertical boundaries, so that colder fluid is located below warmer fluid almost everywhere. Clearly, this stable stratification slows down and suppresses any instability, including the centrifugal one. At the same time, the localized temperature disturbances create local temperature drop in the two horizontal directions, thus creating local nonpotential buoyancy forces. This necessarily leads to the appearance of perturbed vortical motion in all three coordinate planes. The latter is observed in Figs. 7 and 8. This perturbed vortical motion is also suppressed by the stable stratification in the bulk of the flow. At the same time, the perturbed vortical motion in $y = \mathrm{const}$. planes, described by the potential Ψ'_y in Figs. 7 and 8, can speed up the main circulation, thus triggering the centrifugal mechanism again.

To conclude this section, it should be noted that similarity found in disturbance patterns with the fully 2D case [23] and with the case of 2D base flow subject to 3D spanwise-periodic perturbations
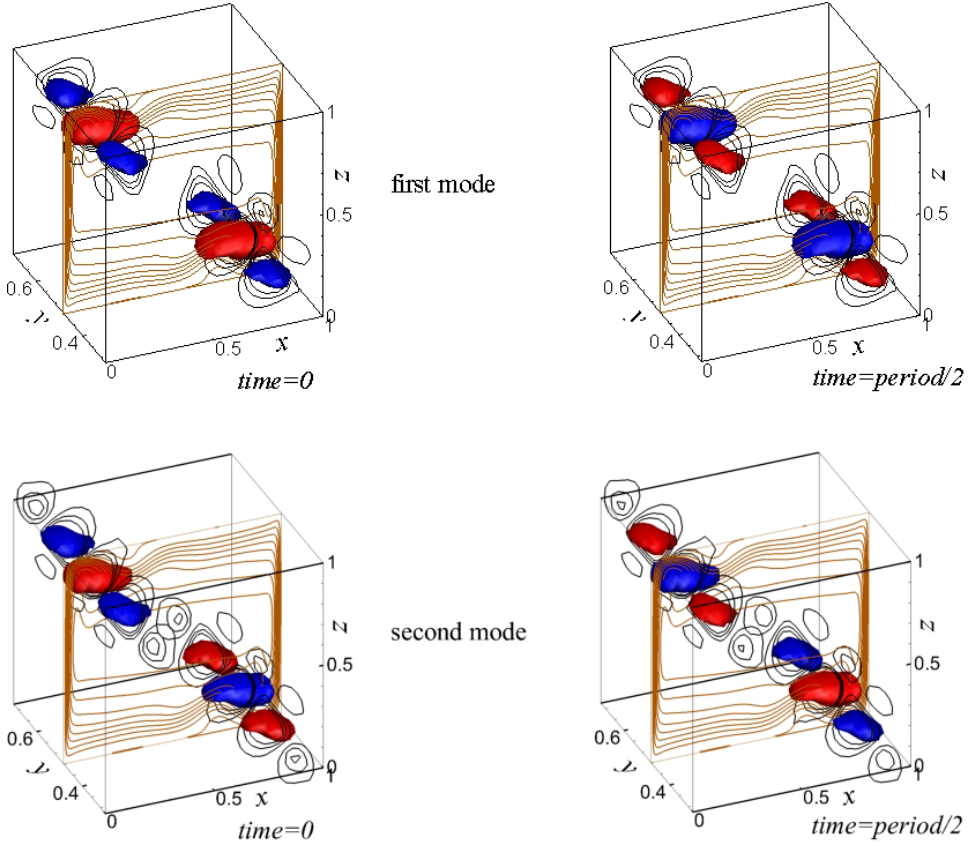
FIG. 11. Snapshots of the potential $\Psi'_z(x', y, z')$ obtained after rotation of coordinates by Eq. (10) shown by colors and black isolines for the two most unstable modes at $Gr = 4.6 \times 10^7$. The snapshots are shown at the beginning and a half of the oscillations period. The brown isolines illustrate the main convective circulation in the midplane $y = 0.5$ defined by the vector potential of the base flow Ψ_y.

[28] allows us to speculate that, in all three cases, the instability sets in owing to the centrifugal mechanism.

3. Slightly supercritical oscillatory states

Fully nonlinear time-dependent calculations were carried out additionally at slight subcriticalities and supercriticalities. The purposes of these calculations were (i) to examine whether the instability is subcritical, which can explain different frequencies of oscillations of the most unstable modes and calculated oscillatory states (Table I); and (ii) to examine whether existence of the two leading eigenmodes can lead to development of different oscillatory states. The time-dependent calculations were done as in Ref. [14]. The time dependencies of the total kinetic energy E_{kin} and the Nusselt number Nu at the hot wall were monitored. They are defined as

$$E_{kin} = \frac{1}{2} \int_V (u^2 + v^2 + w^2) dV, \tag{12}$$

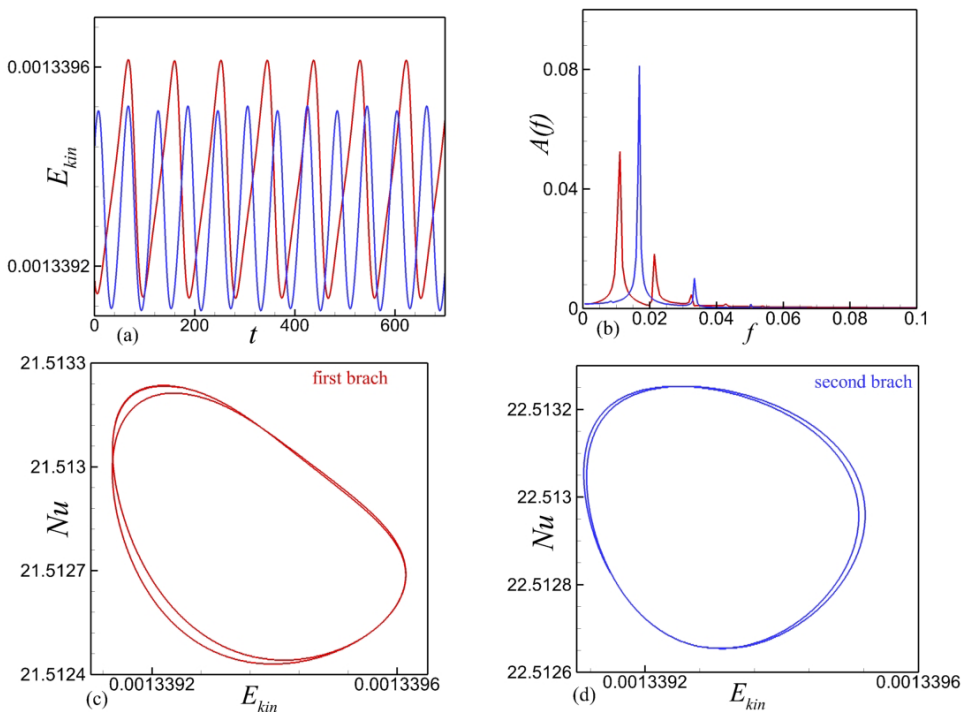$$Nu = \int_0^1 \int_0^1 \left[\frac{\partial T}{\partial x} \right]_{x=0} dy dz. \tag{13}$$

FIG. 12. Two distinct oscillatory flow states at $Gr = 4.6 \times 10^7$. The first and second branches are shown by the red and blue colors, respectively. (a) Histories of the total kinetic energy. (b) Fourier spectrum of the dependencies shown in frame (a). (c) and (d) Phase diagrams plotted in the coordinate kinetic energy $-$ Nusselt number.

The first calculation at $Gr = 4.51 \times 10^7$, which is slightly larger than the critical one, results in finite-amplitude single-frequency oscillations with the dimensionless frequency $\omega \approx 0.0107$. This frequency was reported in Refs. [9,14] as well as in Ref. [11] for the second mode, see Table I. This frequency is larger than the frequencies of the two most unstable modes. There is no evidence of any of the frequencies of the two most unstable modes of the linearized problem. An increase of the Grashof number to $Gr = 4.6 \times 10^7$, which is slightly larger than the critical value of the second most unstable mode (Table I), results in the oscillations with a dominant dimensionless frequency ≈ 0.0167, while a weak peak in the Fourier spectrum is also observed at the dimensionless frequency ≈ 0.00833. To get better insight into the frequency change, we again used the developed oscillatory flow at $Gr = 4.51 \times 10^7$ and performed calculations for $Gr = 4.55 \times 10^7$. These calculations resulted in an oscillatory regime with $\omega \approx 0.0107$. Further increase of the Grashof number to $Gr = 4.6 \times 10^7$ resulted in the oscillatory state with the same frequency. Thus, we obtained two distinct oscillatory states, which are illustrated in Fig. 12. Figure 12(a) shows different time dependencies of the kinetic energy and Fig. 12(b) different frequency spectra calculated from the two signals of Fig. 12(a). Peaks at the reported frequencies and their first harmonics are clearly seen there. Figures 12(b) and 12(c) show phase trajectories plotted in the coordinates (Nu, E_{kin}). We observe two different phase trajectories, which are double tori, obviously produced by the main frequencies and their first harmonics. For the following, we denote the solution branches with the frequencies ≈ 0.01 and ≈ 0.017, as branches 1 and 2, respectively.

Both branches of the periodic oscillatory flows were calculated for a gradually increasing Grashof number until they became chaotic. It was also checked that the solutions of branch 1 are characterized by the 2D rotational symmetry, while the solutions of branch 2 exhibit 3D
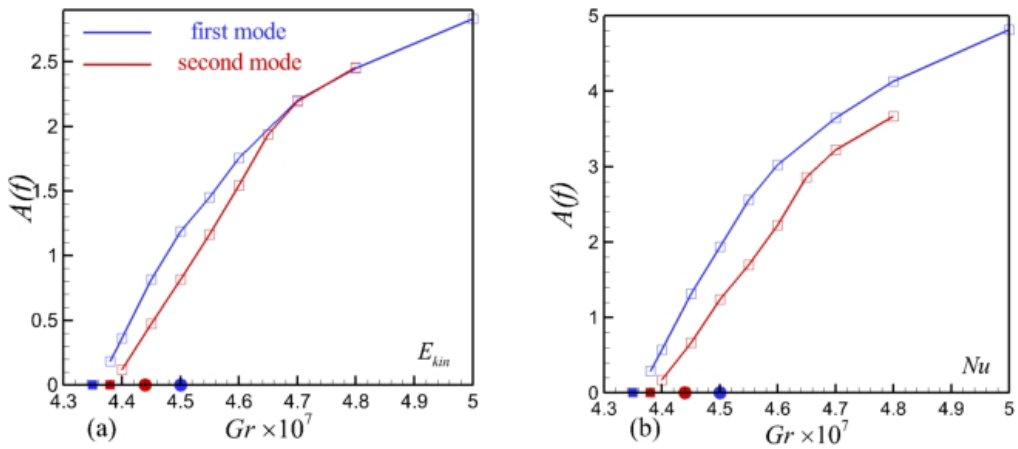
FIG. 13. Amplitudes of first harmonics of the two unstable modes versus the Grashof number for small supercriticalities (lines with empty squares). Filled squares show values of the Grashof number at which time-dependent computation resulted in a steady flow. Filled circles show critical values of the two modes.

centrosymmetry. Amplitudes of the primary harmonics were obtained by applying the Fourier transform and are reported in Fig. 13. One observes that the amplitudes monotonically increase with the Grashof number. The filled squares in Fig. 13 show values of the Grashof number, at which the oscillatory state turned into the steady one when the Grashof number was gradually decreased. These values appear to be smaller than the critical values of the Grashof number reported in Table I and shown by filled circles in Fig. 13. The subcritical character of both bifurcations is clearly seen. These subcriticalities explain why frequencies of the calculated oscillatory flows differ from those predicted by the linear stability analysis.

At $Gr = 5 \times 10^7$, all the symmetries in both branches are broken. The first branch remains periodic, while the second branch becomes chaotic, as is illustrated by phase diagrams in Fig. 14. The phase diagram of the first branch [Fig. 14(a)] is a closed line, which returns to itself after making several loops, thus becoming a multiple torus formed by the main oscillation frequency and its several harmonics. The phase diagram of the second branch [Fig. 14(b)] is an unclosed line localized in space and forming a strange attractor.
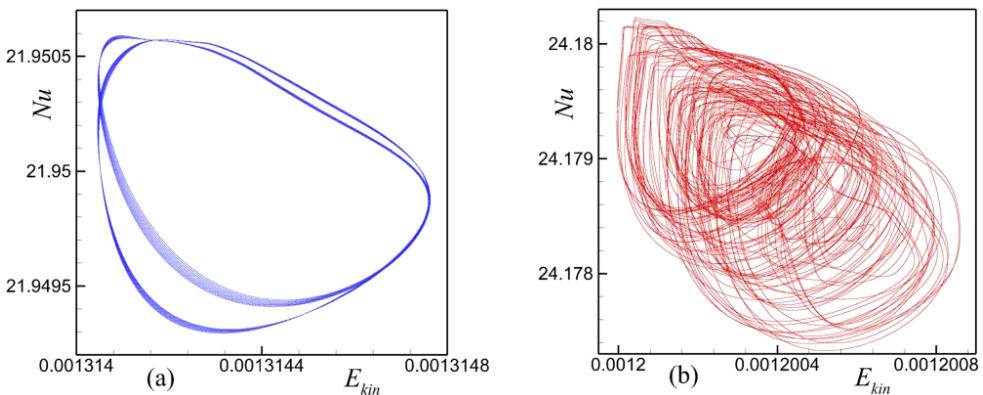

FIG. 14. Phase diagrams of the two time-dependent solution branches plotted in the coordinate kinetic energy − Nusselt number at $Gr = 5 \times 10^7$.
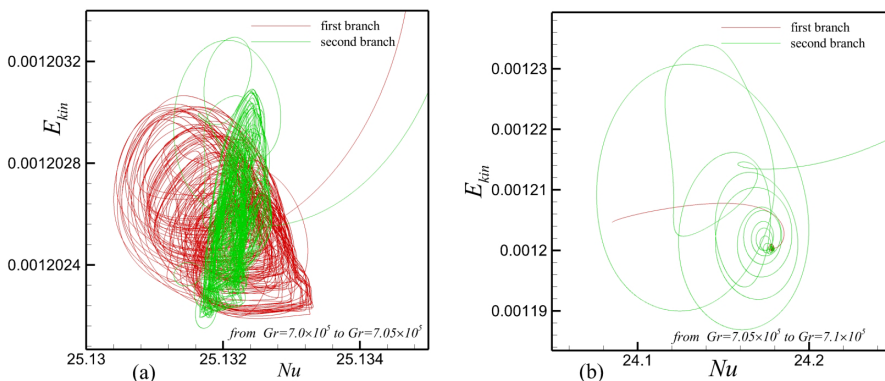
FIG. 15. Phase trajectories in the plane kinetic energy − Nusselt number (a) for the two branches starting from two different stochastic states at 7.0×10^7 and arriving at two different stochastic states at 7.05×10^7, and (b) for the two branches starting from two different stochastic states at 7.05×10^7 (a) and arriving at the same fixed point at 7.1×10^7.

C. Secondary oscillatory-steady bifurcation

As found in Ref. [14], flows exhibiting chaotic oscillations at $Gr > 5 \times 10^7$ become stable and steady when the Grashof number is increased slightly $>7 \times 10^7$ (see fig. 9 in Ref. [14]). Therefore, the next question to study is the following. Do two distinct chaotic states, as described above, arrive at the same steady flow, or one of them arrives at the steady flow, while the other one remains chaotic, regularly oscillating, or arrives at another steady state? The answer to this question is presented in Figs. 15 and 16. In Fig. 15(a), two phase trajectories that start from some point of the two different chaotic solutions at $Gr \approx 7 \times 10^7$ arrive at two different chaotic solutions in their asymptotic states at $Gr \approx 7.05 \times 10^7$. The difference can be easily seen for the different shapes of the attractors, to which the flows arrive at large time. Note that the flows belonging to both chaotic branches remain fully nonsymmetric. Figure 15(b) shows what happens with these two phase trajectories when the Grashof number is further increased to $Gr \approx 7.1 \times 10^7$. We observe that both trajectories arrive at the same stable focus. To illustrate additionally that this is the same steady flow and not two different flows, we plot the corresponding time dependencies in Fig. 16. It is clearly seen there that the solutions, belonging to either of two branches, arrive at the same values of the kinetic energy
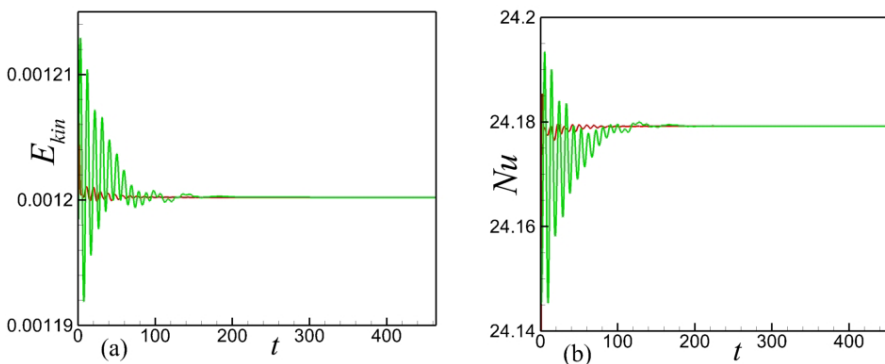

FIG. 16. (a) Time evolution of the kinetic energy and (b) the Nusselt number for the first (red) and second (green) solution branch, when the Grashof number is increased from 7.05×10^7 to 7.1×10^7.
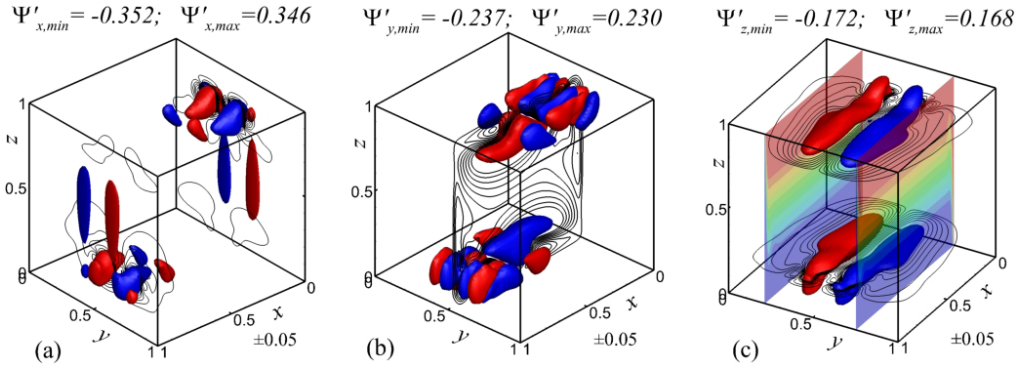
FIG. 17. Perturbation potentials corresponding to the second bifurcation reinstating the stability. $Gr = 7.08 \times 10^7$. The cross-sections in (c) show isotherms equally distributed between the values 0.3 and 0.7. The red color corresponds to larger temperature and the blue color to smaller ones.

and Nusselt number. No oscillatory states are observed beyond $Gr = 7.1 \times 10^7$ until the next critical number is approached (see the next section). These steady flows pertain to all three symmetries.

We discuss further the instability of steady flow at $Gr < 7.1 \times 10^7$ that occurs when the Grashof number is reduced. The calculations show that the leading eigenvalue, which crosses the imaginary axis, is real and single. The instability develops as a transition from the steady state that preserves all three symmetries to a chaotic oscillating state, in which all three symmetries are broken. The latter is confirmed by calculation of the criteria in Eqs. (7)–(9) for the most unstable disturbance as well as for a slightly subcritical oscillatory flow snapshot. The vector potentials of the most unstable disturbance are shown in Fig. 17. Note that, in this case of monotonic instability, the disturbance is a real function. The maximal and minimal values of the potentials indicate a slight break of symmetry, so that the symmetry breaking observed in the unsteady flow is a result of the instability and not a nonlinear effect.

Patterns of the vector potential disturbances (Fig. 17) are located in the same areas as for the primary bifurcation (see Figs. 7 and 8). Despite that the disturbance structures are not same, they exhibit certain similarity, so that we can perform the same analysis and recall the same arguments as for the primary bifurcation in Sec. IV B. Thus, we conclude that this instability also does not develop due to the boundary layers adjacent to the isothermal vertical walls. Furthermore, similarity of the most unstable disturbances leads to an assumption that, also in this case, the instability sets in owing to centrifugal mechanisms. This assumption is supported by the Rayleigh and Bayly criteria (not shown in figures), which appear to be like those observed for the primary bifurcation. Finally, we plot the perturbation potential Ψ'_z in the rotated coordinate system, as in Fig. 13. The result is shown in Fig. 18, where we again observe the vortices located in the upper left and lower right corners and rotating in the diagonal plane. As in the case of the primary bifurcation, this indicates the centrifugal instability mechanism.

To explain why the oscillatory flow stabilizes with the increase of the Grashof number, we recall again that, at large Grashof numbers, the temperature in the bulk of the flow attains a stable stratification, so that colder fluid is located below and warmer fluid above. This is illustrated additionally in the cross-sections of Fig. 17(c). Therefore, with the increase of the Grashof number, the stable stratification becomes steeper which, at some point, stabilizes the flow. When the Grashof number is decreased, the stabilized steady flow becomes unstable owing to a centrifugal mechanism like one that triggers the primary bifurcation. The apparent difference is that this secondary inverse bifurcation cannot be interpreted as a Hopf one because it sets in due to a single real fully nonsymmetric eigenmode. It is most probably a subcritical pitchfork bifurcation in which two
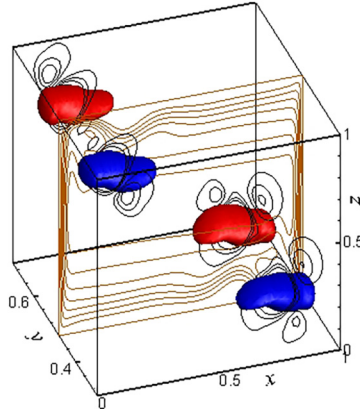
FIG. 18. Snapshots of the potential $\Psi_z'(x', y, z')$ obtained after rotation of coordinates by Eq. (10) shown by colors and black isolines at Gr $= 7.08 \times 10^7$. The brown isolines illustrate the main convective circulation in the midplane $y = 0.5$ defined by the vector potential of the base flow Ψ_y.

subcritical chaotic modes may correspond to the symmetry breaking with a positive or negative amplitude of the real nonsymmetric eigenmode.

D. The third steady-oscillatory transition

The steady flow, whose stability is reinstated at Gr $\approx 7.1 \times 10^7$, preserves all three symmetries until it becomes oscillatory unstable at Gr $\approx 2.8 \times 10^8$. The corresponding most unstable perturbation also exhibits all three symmetries, which is quite unexpected. Isosurfaces of the temperature disturbance are shown in Fig. 19, and the divergence-free velocity potentials in Fig. 20. The corresponding oscillations can be seen better in Animations 5 and 6 in the Supplemental Material [30].

We observe that the disturbances appear in the upper left and lower right corners. At first glance, these disturbances can be interpreted as rolls elongated in the y direction and rotating in the (x, z) planes. However, as is seen from Fig. 20, the intensity of the vortical motions in the two other coordinate planes is of the same order. This means that the instability is entirely 3D and cannot be
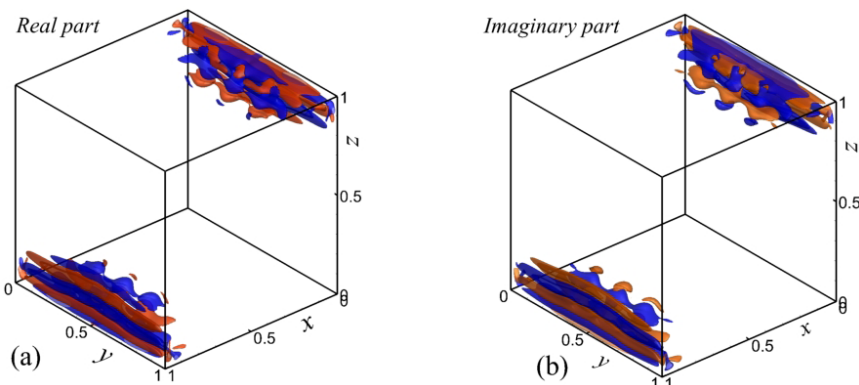

FIG. 19. Real and imaginary parts of two modes of temperature perturbation of the third bifurcation. The isosurfaces are plotted for the levels ± 0.0002, while maximal amplitude value is 0.00384. See Animation 5 in the Supplemental Material [30].
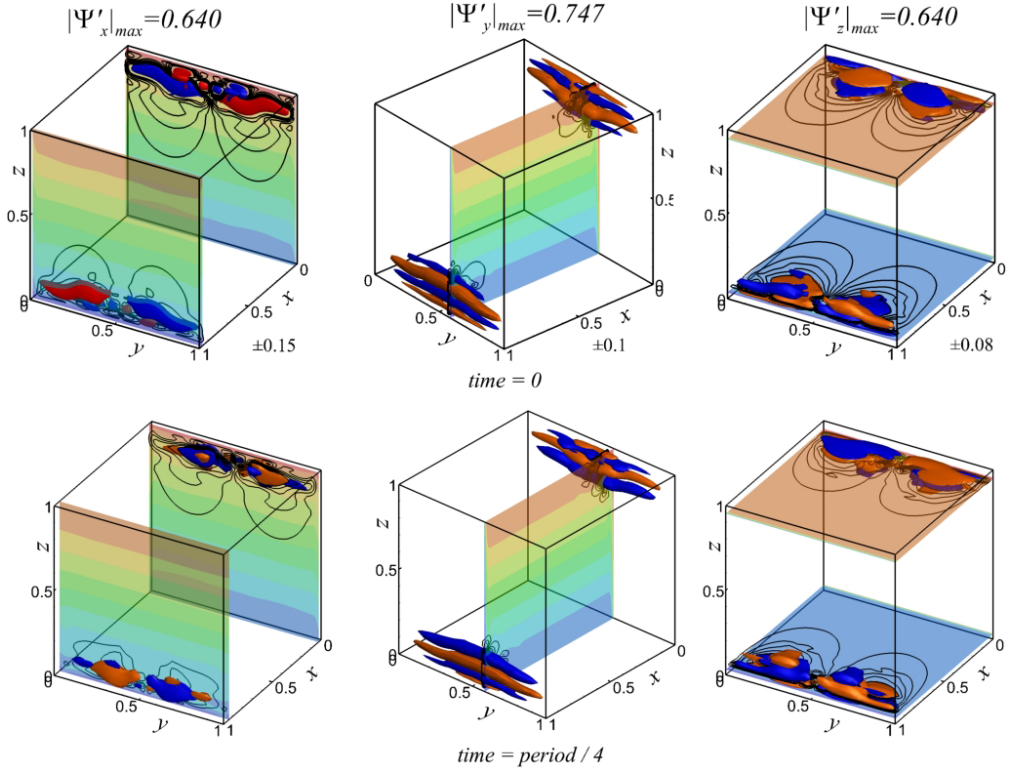
FIG. 20. Snapshots of the velocity potentials of the most unstable perturbation of the third bifurcation at $Gr_{cr} \approx 2.96 \times 10^8$. The minimal and maximal values and the plotted levels are shown in the upper frames. The snapshots at the $\frac{1}{2}$ and $\frac{3}{4}$ of the period can be obtained by reversing the colors. The color maps show the temperature field in the characteristic cross-sections. See Animation 6 in the Supplemental Material [30] for evolution of the perturbation potentials over the period.

explained as a modification of a known 2D one. Thus, we can argue that this is not instability of the boundary layers [9] because the latter is likely to be 2D-like owing to the Squire transformation, which can be applied to isothermal as well as nonisothermal boundary layers. Moreover, and as was mentioned above, the boundary layers are expected to become unstable in the central part of the vertical boundaries, where the shear is larger (see Fig. 20), while the observed instability starts in the corners, is advected along the vertical boundaries, and dissipates well before reaching the boundary middle regions.

We examine the temperature distribution in the upper left and lower right corners (Fig. 3) and find that there is no unstable stratification there. Moreover, the horizontal change of the temperature in these corners appears to be weaker than in the opposite ones. Thus, the onset of instability cannot be attributed to any convective mechanism.

The reverse circulations discussed in Sec. IV B for $Gr = 4.6 \times 10^7$ are also observed at a noticeably larger Grashof number $Gr = 2.96 \times 10^8$, discussed here. They are easily revealed in the vertical velocity profiles that change sign several times along the x direction (Fig. 21). As in the case of the first bifurcation, the reverse circulations are better seen in the streamlines shown in the cross-section $y = 0.5$ together with the 3D isosurfaces of the absolute values (amplitudes) of the vector potential of the most unstable velocity. As in the case of the primary bifurcation, all the amplitudes are of comparable order of magnitude and are located in the areas of reverse circulations.
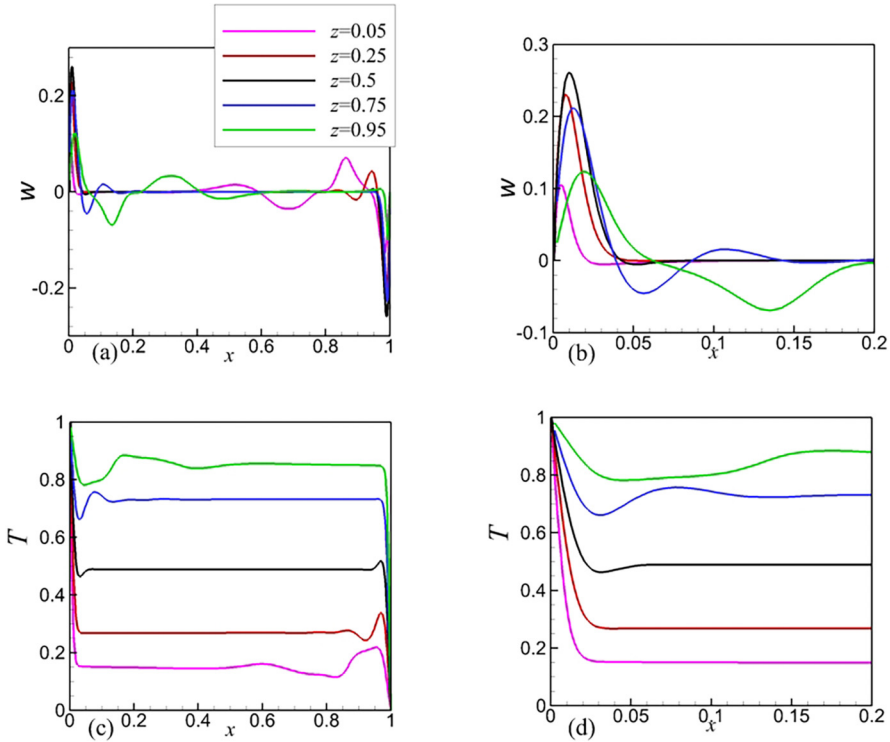
FIG. 21. Profiles of the vertical velocity and the temperature in the spanwise midplane $y = 0.5$. In (b) and (d), the profiles in the interval $0 \leqslant x \leqslant 0.2$ are zoomed. Gr $= 2.89 \times 10^8$.

The Rayleigh criterion for the steady flow at Gr $= 2.96 \times 10^8$ is shown in Fig. 22. The Bayly criterion has a similar pattern and is not shown. The patterns of both criteria are quite like ones observed for the primary and secondary bifurcations. The Rayleigh criterion η changes its sign
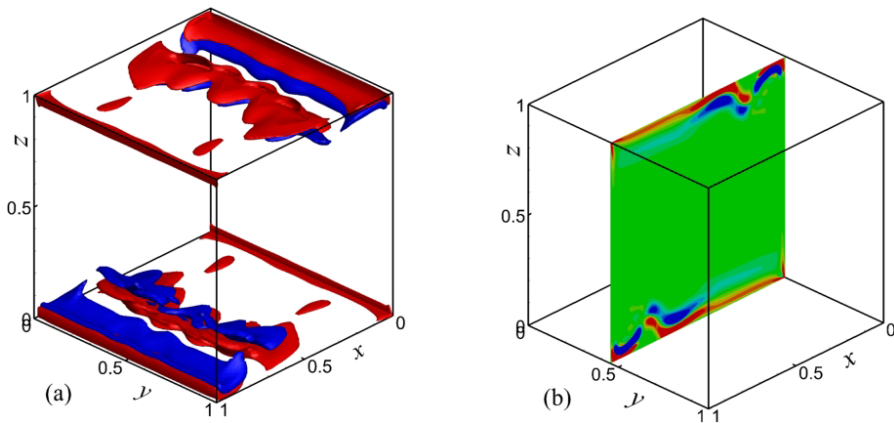

FIG. 22. Isolines of Rayleigh criterion calculated for the base flow at $Gr_{cr} \approx 2.96 \times 10^8$. The level values in (a) are ± 0.03. Positive and negative values are shown by the red and blue color, respectively.
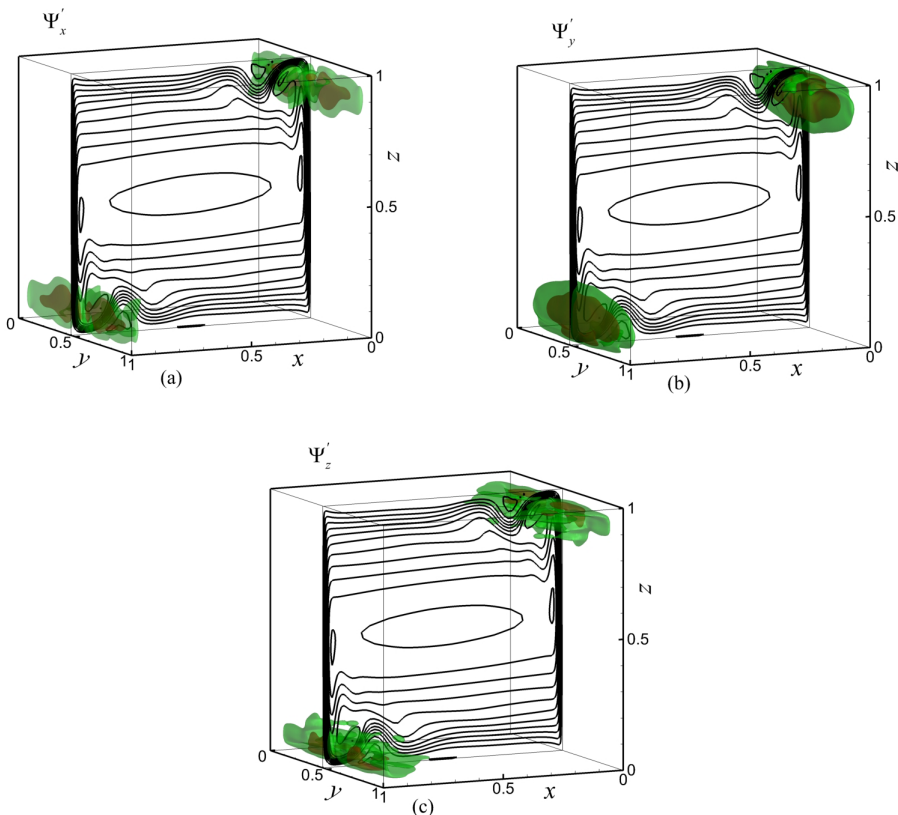
FIG. 23. Absolute values of the velocity potentials of the most unstable perturbation of the third bifurcation (isosurfaces) and isolines of the base flow velocity potential Ψ_y plotted in the center plane $y = 0.5$ at $Gr_{cr} \approx 2.96 \times 10^8$. The isosurfaces are plotted for the levels 0.1 and 0.25. The maximal values of $|\Psi'_x|$, $|\Psi'_y|$, and $|\Psi'_z|$ are 0.640, 0.747, and 0.468, respectively.

from positive to negative in the corner areas, where the Bayly criterion R attains negative values. As above, both criteria indicate the possibility of centrifugal instability.

Following Ref. [22] and Sec. IV B, we calculate the velocity potentials in the rotated coordinate system defined by Eq. (11). Figure 23 shows a snapshot of the potential Ψ'_z in the same way as in Fig. 12. This figure allows one to see vortices located in the diagonal plane shown in the figure, as is expected in the case of centrifugal instability [22]. Amplitudes of the two other velocity potentials are smaller, so that the vortical motion shown in Fig. 24 is dominating. Animation 5 in the Supplemental Material [30] illustrating this instability also shows rotational motion of the perturbation structures in the corners.

As discussed above, if the instability takes place owing to the centrifugal instability mechanism, it must be similar in both upper left and lower right corners, so that the perturbation patterns are symmetric or antisymmetric with respect to the 2D rotation in Eq. (8). The same can be said about the reflection symmetry in Eq. (7). It is noteworthy that the most unstable disturbance in this case preserves both symmetries. The 3D rotation symmetry, being a superposition of the two former symmetries, is also necessarily preserved. Thus, slightly supercritical oscillatory flows can be expected to preserve all three symmetries. The oscillatory flows calculated in Ref. [14] for $Gr = 2.9 \times 10^8$ and 3×10^8 preserve all three symmetries. At the same time, existence of the oscillatory flow at $Gr = 2.9 \times 10^8$, which is slightly smaller than the critical one, indicates the possible subcriticality of this transition.
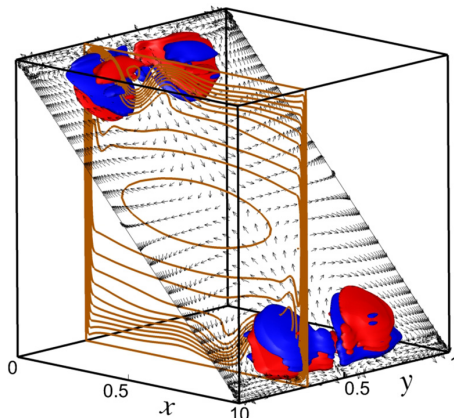
FIG. 24. Snapshot of the potential $\Psi_z'(x', y, z')$ obtained after rotation of coordinates by Eq. (10) shown by colors and black isolines for the most unstable mode at Gr $= 2.96 \times 10^8$. The snapshots are shown at the beginning and a half of the oscillation period. The brown isolines illustrate the main convective circulation in the midplane $y = 0.3$ defined by the vector potential of the base flow Ψ_y.

V. CONCLUDING REMARKS

We revisited the problem of linear stability of 3D buoyancy convection flow in a laterally heated cubical cavity with perfectly insulated horizontal and spanwise boundaries. This problem was considered in several studies by time-dependent calculations [9–14], where primary steady-oscillatory transition was mainly addressed. The reported results exhibited a noticeable scatter in values of the critical Grashof number as well as in the frequency of appearing oscillations. Time-dependent calculations in Ref. [11] reported two different eigenmodes with quite close critical Grashof (Rayleigh, Ra = GrPr) numbers; however, this issue since then was never addressed. Later time-dependent calculations in Ref. [14] argued that, with the increase of the Grashof number, the primary oscillatory instability is followed by flow stabilization, and another steady-oscillatory transition takes place at a much larger Grashof number.

In this paper, we applied a linear stability analysis to the problem and arrived at converged values of the critical Grashof number and critical frequency, which are reported and compared with the previous studies in Table I. Furthermore, we confirmed the results in Ref. [11] by computing the two distinct eigenmodes. We discussed their symmetries and argued for the physical reasons that may cause instability due to either of the modes. Applying full 3D time-dependent calculations again, we have shown that steady-oscillatory transitions due to either of the modes are subcritical. We also confirmed existence of the chain of bifurcations, so that primary steady-oscillatory transition takes place at Gr $\approx 4.5 \times 10^7$, then the stability reinstates at Gr $\approx 7 \times 10^7$, and the flow becomes oscillatory unstable again at Gr $\approx 2.8 \times 10^8$.

It was shown that time development of the two distinct most unstable eigenmodes result in two different oscillatory solutions that, at small supercriticalities, preserve the modes symmetries and, with further increase of the Grashof number, break all the symmetries and become chaotic. However, when the Grashof number approaches a value of 7×10^7, they arrive at a single steady state, which exhibits all the initial symmetries and is a stable focus in the phase space.

To gain some more insight into the physical mechanisms that trigger the bifurcations, we analyzed the patterns of flows at the critical Grashof numbers and patterns of the most unstable disturbances. We argue that the main destabilizing mechanism is centrifugal, which is stabilized by the stable temperature stratification that develops in the bulk of the flow. We have argued that reverse circulations appearing at the horizontal boundaries increase curvature of the streamlines of the main

convective circulations, which makes the centrifugal destabilizing mechanism stronger. These three factors appear to be present in all three transitions.

ACKNOWLEDGMENTS

---

[1] G. De Vahl Davis, Natural convection of air in a square cavity, a benchmark solution, Int. J. Numer. Meths. Fluids **3**, 249 (1982).

[2] M. Lappa, *Thermal convection, Patterns, Evolution and Stability* (Wiley & Sons, Singapore, 2009).

[3] T. Fusegi, J. M. Hyun, K. Kuwahara, and B. Farouk, A numerical study of three dimensional natural convection in a differentially heated cubical enclosure, Int. J. Heat Mass Transfer **34**, 1543 (1991).

[4] E. Tric, G. Labrosse, and M. Betrouni, A first inclusion into the 3D structure of natural convection of air in a differentially heated cavity, from accurate numerical solutions, Int. J. Heat Mass Transfer **43**, 4043 (1999).

[5] B. A. V. Bennet and J. Hsueh, Natural convection in a cubic cavity, implicit numerical solution of two benchmark problems, Numer. Heat Transfer, Part A **50**, 99 (2006).

[6] Y. Peng, C. Shu, and Y. T. Chew, A 3D incompressible thermal lattice Boltzmann model and its application to simulate natural convection in a cubic cavity, J. Comput. Phys. **193**, 260 (2003).

[7] S. Wakashima and T. S. Saitoh, Benchmark solutions for natural convection in a cubic cavity using the high-order time-space method, Int. J Heat. Mass Transfer **47**, 853 (2004).

[8] Y. Feldman and A. Y. Gelfgat, On pressure-velocity coupled time-integration of incompressible Navier-Stokes equations using direct inversion of Stokes operator or accelerated multigrid technique, Comput. Struct. **87**, 710 (2009).

[9] R. J. A. Janssen and R. A. W. M. Henkes, Instabilities in three-dimensional differentially-heated cavities with adiabatic horizontal walls, Phys. Fluids **8**, 62 (1996).

[10] G. Labrosse, E. Tric, H. Khallouf, and M. Betrouni, A direct (pseudo-spectral) solver of the 2D/3D Stokes problem: Transition to unsteadiness of natural-convection flow in a differentially heated cubical cavity, Numer. Heat Transfer, Pt. B **31**, 261 (1997).

[11] G. De Gassowski, S. Xin, O. Daube, and Y. Fraigneau, Bifurcations and multiple solutions in an air-filled differentially heated cubic cavity, International Heat Transfer Conference 13 (2006), Begel House, Danbury, Connecticut, United States, https://publons.com/wosop/publisher/216/begell-house, doi:10.1615/IHTC13.p1.50.

[12] T. W.-H. Sheu and R.-K. Lin, Three-dimensional bifurcations in a cubic cavity due to buoyancy-driven natural convection, Int. J. Heat Mass Transfer **54**, 447 (2011).

[13] L. Soucasse, Ph. Riviére, A. Soufani, S. Xin, and P. Le Quéré, Transitional regimes of natural convection in a differentially heated cubical cavity under the effects of wall and molecular gas radiation, Phys. Fluids **26**, 024105 (2014).

[14] A. Y. Gelfgat, Time-dependent modelling of oscillatory instability of three-dimensional natural convection of air in a laterally heated cubic box, Theor. Comput. Fluid Dyn. **31**, 447 (2017).

[15] A. Y. Gelfgat, Instability of natural convection in a laterally heated cube with perfectly conducting horizontal boundaries, Theor. Comput. Fluid Dyn. **34**, 693 (2020).

[16] A. Y. Gelfgat, Instability of natural convection of air in a laterally heated cube with perfectly insulated horizontal boundaries and perfectly conducting spanwise boundaries, Phys. Rev. Fluids **5**, 093901 (2020).

[17] H. Ferialdi, M. Lappa, and C. Haughey, On the role of thermal boundary conditions in typical problems of buoyancy convection: A combined experimental-numerical analysis, Int. J. Heat Mass Transfer **159**, 120012 (2020).

[18] A. L. Yarin, T. A. Kowalewski, W. J. Hiller, and St. Koch, Distribution of particles suspended in convective flow in differentially heated cavity, Phys. Fluids **8**, 1130 (1996).

[19] A. Juel, T. Mullin, H. Ben Hadid, and D. Henry, Three-dimensional free convection in molten gallium, J. Fluid Mech. **436**, 267 (2001).

[20] B. Hof, A. Juel, L. Zhao, D. Henry, H. Ben Hadid, and T. Mullin, On the onset of oscillatory convection in molten gallium, J. Fluid Mech. **515**, 391 (2004).

[21] J. A. Scott, An Arnoldi code for computing selected eigenvalues of sparse real unsymmetric matrices, ACM Trans. Math. Software **21**, 432 (1995).

[22] A. Y. Gelfgat, Linear instability of the lid-driven flow in a cubic cavity, Theor. Comput. Fluid Dyn. **33**. 59 (2019).

[23] A. Y. Gelfgat, Stability of convective flows in cavities: Solution of benchmark problems by a low-order finite volume method, Int. J. Numer. Meths. Fluids **53**, 485 (2007).

[24] A. Y. Gelfgat, Visualization of three-dimensional incompressible flows by quasi-two-dimensional divergence-free projections, Comput. Fluids **97**, 143 (2014).

[25] A. Y. Gelfgat, Visualization of three-dimensional incompressible flows by quasi-two-dimensional divergence-free projections in arbitrary flow regions, Theor. Comput. Fluid Dyn. **30**, 339 (2016).

[26] W. J. Hiller, St. Koch, and T. A. Kowalewski, Three-dimensional structures in laminar natural convection in a cubic enclosure, Exp. Thermal Fluid Sci. **2**, 34 (1989).

[27] P. J. Roache, Perspective: A method for uniform reporting of grid refinement studies, J. Fluids Eng. **116**, 405 (1994).

[28] S. Xin and P. Le Quéré, Stability of two-dimensional (2D) natural convection flows in air-filled differentially heated cavities: 2D/3D disturbances, Fluid Dyn. Res. **44**, 031419 (2012).

[29] R. Purgolesi and E. Leriche, Proper orthogonal decomposition of a fully confined cubical differentially heated cavity flow at Rayleigh number Ra = 10^9, Comput. Fluids **61**, 14 (2012).

[30] See Supplemental Material at http://link.aps.org/supplemental/10.1103/PhysRevFluids.8.043902 for Animations 1–6.

[31] S. Ostrach, An analysis of laminar free convection flow and heat transfer about a flat plate parallel to the direction of the generating body force, NACA Report 1111 (1953), http://ntrs.nasa.gov/archive/nasa/casi.ntrs.nasa.gov/19930092147.pdf.

[32] R. Janssen and S. Armfield, Stability properties of the vertical boundary layers in differently heated cavities, Int. J. Heat and Fluid Flow **17**, 547 (1996).

[33] H. Yahata, Stability analysis of natural convection evolving along a vertical heated plate, J. Phys. Soc. Jpn. **70**, 111 (2001).

[34] G. P. Klaassen and W. R. Peltier, The onset of turbulence in finite-amplitude Kelvin-Helmholtz billows, J. Fluid Mech. **155**, 1 (1985).

[35] A. Y. Gelfgat and E. Kit, Spatial versus temporal instabilities in a parametrically forced stratified mixing layer, J. Fluid Mech. **552**, 189 (2006).

[36] M. R. Ravi, R. A. W. M. Henkes, and C. J. Hoogendoorn, On the high Rayleigh number structure of steady laminar natural-convection flow in a square enclosure, J. Fluid Mech. **262**, 325 (1994).

[37] B. J. Bayly, Three-Dimensional Instability of Elliptical Flow, Phys. Rev. Lett. **57**, 2160 (1986).

[38] B. J. Bayly, Three-dimensional centrifugal-type instabilities in inviscid two-dimensional flows, Phys. Fluids **31**, 56 (1988).

[39] S. Albensoeder, H. C. Kuhlmann, and H. J. Rath, Three-dimensional centrifugal-flow instabilities in the lid-driven-cavity problem, Phys. Fluids **13**, 121 (2001).

[40] www.westgrid.ca.

[41] www.computecanada.ca.